


Article

Design and Stiffness Evaluation of a Compliant Joint with Parallel Architecture Realizing an Approximately Spherical Motion

Farid Parvari Rad ¹, Rocco Vertechy ², Giovanni Berselli ^{3,*}  and Vincenzo Parenti-Castelli ²

¹ Prodevco Robotic Solutions, Concord, ON L4K 2P5, Canada; farid.parvarirad@burncomfg.com

² Department of Industrial Engineering, University of Bologna, Via Zamboni, 33, I-40136 Bologna, Italy; rocco.vertechy@unibo.it (R.V.); vincenzo.parenti@unibo.it (V.P.-C.)

³ Department of Mechanical, Energy, Management and Transportation Engineering, University of Genova, Via Balbi, 5, 16126 Genova, Italy

* Correspondence: giovanni.berselli@unige.it; Tel.: +39-335-8092-364

Received: 18 February 2018; Accepted: 21 April 2018; Published: 27 April 2018



Abstract: This paper introduces the design of a fully-compliant Spherical Joint (SJ), obtained by the in-parallel connection of two identical open chains each composed of three equal circular flexible beams, having coincident centers of curvature and mutually orthogonal axes of minimum rotational stiffness. Thanks to its particular topology, the SJ provides a fully isotropic behavior, the two chains being placed in space so as to be symmetric with respect to the beams' center of curvature. At first, the overall system compliance matrix is derived by means of an analytical procedure, in order to obtain a parametric formulation of the SJ behavior within the small deflection range. Then, after finite element validation of the analytical model, an optimization study of the beam geometry is developed, with the aim of maximizing the ratio between the SJ primary to secondary compliance factors. At last, the potential advantages and drawbacks of the proposed design are discussed by numerically evaluating the joint performance in terms of parasitic motions within the large deflection range (namely, when large external loads are applied to the envisaged center of spherical motion).

Keywords: compliant mechanisms/actuators; spherical joint; circular flexible beams; compliance matrix; finite element analysis; design graphs

1. Introduction

A Compliant Mechanism (CM) may be defined as a single- or multi-piece flexible device that can provide both the mobility of a traditional rigid-link mechanism and the stiffness of a conventional structure [1,2]. However, since CMs are designed and manufactured in order to transfer specific motions and forces via the deflection of elastic segments, the structural deformation along some selected directions is actually considered a desirable feature. In practice, CMs represent an elegant solution for designers that are willing to replace rigid links connected through traditional kinematic pairs (e.g., pins, cams and sliders) with deformable members. Surely, traditional joints can supply nearly infinite compliance along a given set of axes and rather large stiffness along any other direction. Nonetheless, some unavoidable issues when using these types of kinematic pairs are, for instance, clearance and friction, which may critically affect the accuracy and dynamic behaviour of any device requiring high speed, precision and efficiency [3–5]. In all these cases, a CM-based design may lead to performance improvements due to the absence of contacts between rigid surfaces and the consequent reduction of wear, need for lubrication and backlash, thus potentially improving the mechanism precision [6]. Other possible CM advantages are the capability to store elastic energy, which can be

beneficial in those mechanical devices (such as robotic compliant actuators [7–9]) that need to be equipped with return springs [10,11], and the reduced number of parts (ideally, monolithic solutions can be conceived and prototyped [12,13]). This latter property is also closely connected to potentials for weight and assembly-cost reductions. In particular, CMs may be envisaged as a promising paradigm to enable the *Design For No-Assembly* concept and, according to [14], they become ideal candidates for the development of high-precision manipulators when driven by high-resolution positioning actuators (such as piezoelectric or electromagnetic motors [15–17]). Nonetheless, aside these numerous advantages, a series of challenging issues must be considered, namely: (a) continuous rotational motions cannot be achieved by means of flexible members; (b) in many applications, CM resistance to fatigue must be carefully addressed; (c) the analysis and design of CMs is more complex when compared to traditional mechanisms; (d) differently from rigid-link mechanisms, CMs may actually be subjected to non negligible deformations also along undesired directions. In particular, briefly recalling some basic notation previously proposed in [18], flexible segments composing a generic CM may be conceived to allow for one or more *primary displacement*, namely a Degree of Freedom (DoF) along a desired reference direction, when subjected to a *primary load* acting along the same direction. The term *primary compliance* is actually used to indicate the ratio between any primary displacement and its related primary load. Therefore, flexible members that are conceived to provide multiple DoF will be characterized by high primary compliance factors related to each desired DoF. As an example, let one consider straight slender beams with cylindrical cross section, which have been previously employed in place of spherical rigid pairs [19]. *Parasitic effects* (or *secondary displacements* [20–22]) are rotations or translations (due to presence of axis drift or unforeseen external loads), which are undesirable and shall be minimized whenever possible. Within the small deflection range, parasitic effects can be quantified by means of *secondary compliance factors* (namely, those terms in the compliance matrix that are not regarded as principal compliances). In the literature, as widely known (see e.g., [23,24]), a given CM topology is said to provide a *selectively compliant behavior* if it maintains large primary compliance factors but small secondary compliances.

From what concerns other basic terminology, also adopted in [25], generic CMs may be classified into three categories: *flexure-based CMs*, *flexible beam-based CMs* and *fully compliant elastic continua*. Flexure-based CMs, also called *lumped CM*, are deformable structures whose elastic deflections are localized in "small regions", usually referred to as flexural hinge (or simply flexures). In their most common embodiment design, flexures are obtained by machining one or two cutouts in a constant-width material, making it possible to obtain (if desired) monolithic solutions. Usually, these small-length deformable segments mimic the behavior of a revolute joint and can be characterized by profiles of several shapes. For instance, compliance equations for corner-filletted, parabolic and elliptical flexural hinges are provided in [26–28], whereas a generalized model for various hinge profiles is reported in [29]. Although several flexures may be easily arranged so as to design spatial CMs, their behavior is mostly optimized in order to generate a single DoF, so that the accuracy of rotation is considered as a performance metric and displacements of the flexure midpoint are considered as parasitic effects [30,31]. As for the other CM typologies, flexible beam-based CM and fully compliant elastic continua both belong to the class of *distributed CMs*, where the structure mobility is achieved via a deformation that is evenly distributed over major areas of the structure itself. The first term is employed whenever the CM is designed using slender beam-like segments (which are investigated also in classical books such as [32]), whereas the second term describes CMs providing distributed compliance along complex shapes (also possibly including shell or plate elements), which are specifically designed and optimized to undergo a desired deformation upon the application of known external loads. Distributed CMs may be preferred over lumped CMs since a localized deformation on the flexure region may induce rather high stress concentrations, thus limiting the CM load-bearing capacity, fatigue resistance and motion range. On the other hand, a distributed compliance increases the issues related to parasitic effects, which should be carefully taken into account for design purposes.

In the present work, attention is focused on a particular class of beam-based CM, namely the so-called spherical CMs [33], in which all the points of an end-link are ideally constrained to move on concentric spherical surfaces that are fixed with respect to a ground link, with the spheres' centroid being defined as the center of spherical motion. As for previous attempts to provide this type of motion via compliant structures, a bistable spherical CM has been presented in [34], where a pseudo-rigid body model has been used to analyze seven versions of the device, each comprising joints of different length. In a similar direction, a spherical lamina-emergent CM has been proposed in [35], the main purpose being to obtain a compliant mechanical device fabricated from planar materials, although providing motions out of the fabrication plane. In addition, as a possible application of spherical CMs, a compliant Cardan joint has been proposed in [36], whereas possible CM topologies providing an homokinetic coupling (e.g., double Hook's joint CM) have been reviewed in [37].

In any case, most of the previous literature reports about spherical CMs that have been realized via the connection of flexures ideally behaving as revolute joints (i.e., conceived for planar applications) or straight beams with circular cross section employed in place of a spherical kinematic pair. On the other hand, as previously shown in [38], Circular Flexible Beams (CFBs) with rectangular cross-section and featuring lower rotational rigidity along the radial direction, may be better suited for realizing spherical motions. For instance, a comparative evaluation of the parasitic effects for a spherical CM composed by the in-series connection of either three CFBs or three straight-beam flexures has been reported in [39]. Building on the results of such previous work, this paper proposes a novel architecture for a SJ composed by the in-parallel connection of two identical CFB-based serial chains, each composed of three equal CFBs. Overall, the SJ is designed so that: (1) the curvature centers of the CFBs are all coincident with the desired center of spherical motion; (2) the two CFB-based serial chains are located in space so that each flexure comprises an identical counterpart, symmetrically placed with respect to the plane perpendicular to the axis of principal compliance of the considered flexure. A possible SJ embodiment design is reported in Figure 1, whereas Figures 2 and 3 depict the geometric parameters of both a single CFB and a single serial chain formed by three identical CFBs. Besides the introduction of this SJ design, the main contributions of the present paper are as follows:

- Analytical computation of the SJ compliance matrix and its subsequent diagonalization via Euclidean transformations;
- Validation of the analytical model via Finite Element Analysis (FEA) within the small deflection hypothesis;
- Extension of the numerical results in the large deflection range, results being provided via a set of normalized design graphs that allow to clearly spot the optimal CFB geometric parameter for a reduced SJ parasitic behavior.

Benefits of the proposed architecture include the capability to provide an isotropic behavior (when small external moments are applied to the output link, see Figure 3), which may be of practical use in precision compliant actuators where the absence of unforeseen external loads can be guaranteed. In addition, also considering applications requiring larger motions [40], the SJ may be employed in contact-aided CMs [41,42], thus mitigating the unavoidable translations of the joint center. The rest of the paper is organized as follows: Section 2 briefly presents background theory concerning the computation of compliance and stiffness matrices for flexure-based systems and recalls the results concerning the CFB depicted in Figure 2; Section 3 reports about the analytical model of the proposed SJ, along with the procedure for the compliance matrix diagonalization; Section 4 provides both the FEA validation of the small deflection model and the numerical computations of the SJ behavior in the large deflection range. At last, Section 5 draws the concluding remarks.

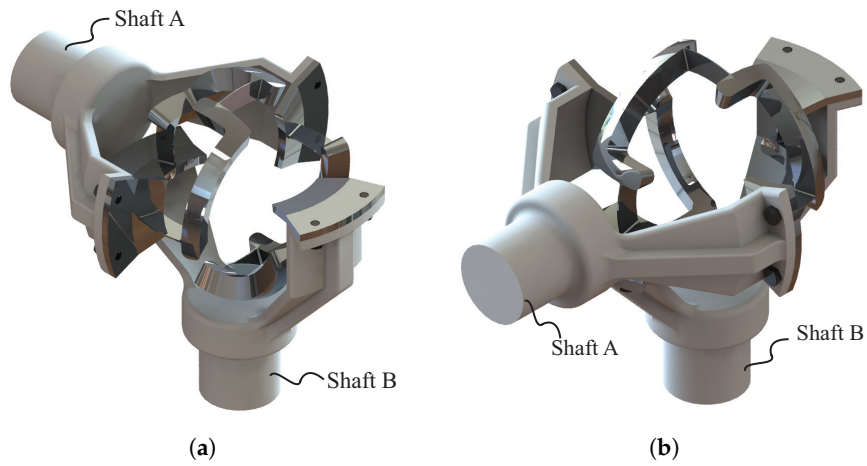


Figure 1. CAD model of a possible embodiment design of the fully-compliant spherical joint composed of two spherical serial chains: isometric views, (a,b), from different angles.

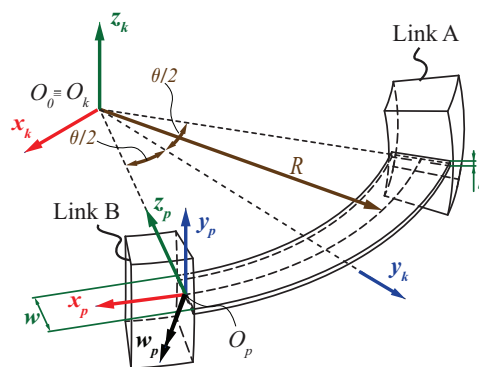


Figure 2. Circular Flexible Beam geometric parameters ($k = 0, 1, 2$).

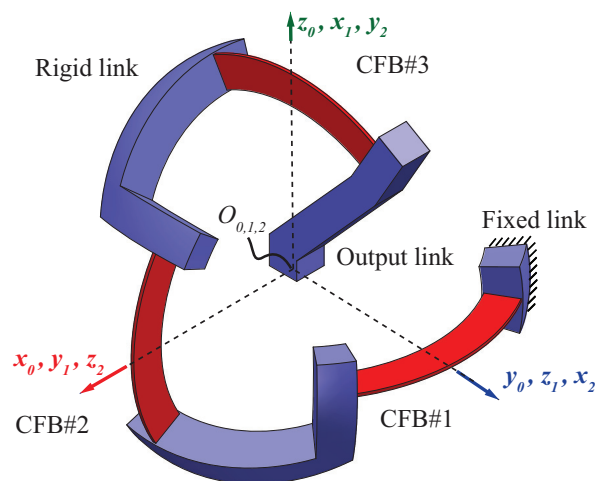


Figure 3. CFB-based spherical open chain.

2. Analytical Design of Flexible Beam-Based Systems: Background Theory

As is known (see e.g., [43–45]), the small deflection behavior of either a single slender beam or a flexure-based system in the proximity of an unloaded configuration can be described in terms of a stiffness matrix or, equivalently, of a compliance matrix, whose definitions are hereafter briefly recalled. Let us first underline that, in the following, the left superscript of a vector or a matrix will denote the coordinate frame in which its components are expressed, whereas T will denote a vector (or matrix) transpose. Let us then consider a single slender beam (such as the CFB schematized in Figure 2), connecting a fixed rigid link A to a movable rigid link B and loaded by an external wrench, ${}^p\mathbf{w} = [{}^p\mathbf{f} \quad {}^p\mathbf{m}]^T$, acting on a point O_p of link B . This external wrench is composed of a force vector, ${}^p\mathbf{f} = [{}^p f_x \quad {}^p f_y \quad {}^p f_z]^T$, and a torque vector, ${}^p\mathbf{m} = [{}^p m_x \quad {}^p m_y \quad {}^p m_z]^T$, whose components are expressed with respect to a generic end link coordinate frame S_p (with axes x_p, y_p, z_p and origin at point O_p). The corresponding small displacement, representing the link B deflection due to the applied load, can be expressed via the vector ${}^p\mathbf{s} = [{}^p\mathbf{u} \quad {}^p\boldsymbol{\theta}]^T$, which is composed of an infinitesimal translation, ${}^p\mathbf{u} = [{}^p u_x \quad {}^p u_y \quad {}^p u_z]^T$, and an infinitesimal rotation, ${}^p\boldsymbol{\theta} = [{}^p \theta_x \quad {}^p \theta_y \quad {}^p \theta_z]^T$, measured in the same coordinate frame S_p . The relations between ${}^p\mathbf{w}$ and ${}^p\mathbf{s}$ can be expressed as:

$${}^p\mathbf{w} = \begin{bmatrix} {}^p\mathbf{f} \\ {}^p\mathbf{m} \end{bmatrix} = \begin{bmatrix} {}^p\mathbf{K}_{fu} & {}^p\mathbf{K}_{f\theta} \\ {}^p\mathbf{K}_{mu} & {}^p\mathbf{K}_{m\theta} \end{bmatrix} \cdot \begin{bmatrix} {}^p\mathbf{u} \\ {}^p\boldsymbol{\theta} \end{bmatrix} = {}^p\mathbf{K} \cdot {}^p\mathbf{s}, \text{ where } {}^p\mathbf{K}_{fu} = {}^p\mathbf{K}_{fu}^T, {}^p\mathbf{K}_{m\theta} = {}^p\mathbf{K}_{m\theta}^T, {}^p\mathbf{K}_{mu} = {}^p\mathbf{K}_{f\theta}^T, \quad (1a)$$

$${}^p\mathbf{s} = \begin{bmatrix} {}^p\mathbf{u} \\ {}^p\boldsymbol{\theta} \end{bmatrix} = \begin{bmatrix} {}^p\mathbf{C}_{uf} & {}^p\mathbf{C}_{um} \\ {}^p\mathbf{C}_{\theta f} & {}^p\mathbf{C}_{\theta m} \end{bmatrix} \cdot \begin{bmatrix} {}^p\mathbf{f} \\ {}^p\mathbf{m} \end{bmatrix} = {}^p\mathbf{C} \cdot {}^p\mathbf{w}, \text{ where } {}^p\mathbf{C}_{uf} = {}^p\mathbf{C}_{uf}^T, {}^p\mathbf{C}_{\theta m} = {}^p\mathbf{C}_{\theta m}^T, {}^p\mathbf{C}_{um} = {}^p\mathbf{C}_{\theta f}^T. \quad (1b)$$

The symbols ${}^p\mathbf{K}$ and ${}^p\mathbf{C} = {}^p\mathbf{K}^{-1}$ respectively denote the beam 6×6 stiffness and compliance matrices, both comprising entries of non uniform physical dimensions. In fact, note that ${}^p\mathbf{K}_{fu}, {}^p\mathbf{K}_{mu}, {}^p\mathbf{K}_{f\theta}, {}^p\mathbf{K}_{m\theta}$ are 3×3 matrices composed of entries with dimensions $[\text{N/m}], [\text{N}], [\text{N/rad}], [\text{Nm/rad}]$ and, similarly, ${}^p\mathbf{C}_{uf}, {}^p\mathbf{C}_{um}, {}^p\mathbf{C}_{\theta f}, {}^p\mathbf{C}_{\theta m}$ are 3×3 matrices composed of entries with dimensions $[\text{m/N}], [1/\text{N}], [\text{rad/N}], [\text{rad/Nm}]$.

Let us now consider a fully-compliant mechanism composed of both in-parallel and in-series combinations of n flexible members, each being described by a stiffness (or compliance) matrix referred to a set of n coordinate frames S_p , for $p = 1 \dots n$. As shown in e.g., [43], once expressed in a common reference frame (such as, for instance, S_0), stiffness matrices can be added to represent parallel combinations, whereas compliance matrices can be added to represent series combinations. Specifically, the overall stiffness of a collection of n in-parallel connected flexible beams or, respectively, the overall compliance of n in-series connected beams can be found as:

$${}^0\mathbf{K} = \sum_{p=1}^n {}^0\mathbf{T}_p \cdot {}^p\mathbf{K} \cdot {}^0\mathbf{T}_p^T, \text{ where } {}^0\mathbf{T}_p = \begin{bmatrix} {}^0\mathbf{R}_p & \mathbf{0} \\ {}^0\tilde{\mathbf{r}}_p \cdot {}^0\mathbf{R}_p & {}^0\mathbf{R}_p \end{bmatrix} \quad (\text{for in-parallel connections}), \quad (2a)$$

$${}^0\mathbf{C} = \sum_{p=1}^n {}^0\mathbf{T}_p^{-T} \cdot {}^p\mathbf{C} \cdot {}^0\mathbf{T}_p^{-1} = \sum_{p=1}^n {}^p\mathbf{T}_0^T \cdot {}^p\mathbf{C} \cdot {}^p\mathbf{T}_0 \quad (\text{for in-series connections}). \quad (2b)$$

The symbols ${}^0\mathbf{T}_p$ and ${}^0\mathbf{R}_p$ respectively denote the 6×6 adjoint matrix and the 3×3 rotation matrix of frame S_p with respect to frame S_0 , whereas ${}^0\tilde{\mathbf{r}}_p$ denotes the skew symmetric matrix of the position vector ${}^0\mathbf{r}_p$, which locates the origin of frame S_p with respect to frame S_0 . Each term in the sum, namely ${}^0\mathbf{T}_p \cdot {}^p\mathbf{K} \cdot {}^0\mathbf{T}_p^T$ (or, respectively, ${}^p\mathbf{T}_0^T \cdot {}^p\mathbf{C} \cdot {}^p\mathbf{T}_0$) simply relates each matrix previously computed in the generic frame S_p to the new frame S_0 . Note that mixed combinations of parallel and series generalized spring-like elements require similar groups to be combined first then inverted as necessary to complete the combination. For spherical CMs like those considered here and depicted in Figures 1–3, made by the connection of CFBs with coincident centers coinciding with the desired center of spherical motion,

O_0 , a suitable frame is the one having origin at O_0 and with axes suitably defined in order to obtain (if possible) a diagonal compliant matrix [46], hereafter referred to as ${}^d\mathbf{C}$. In this particular frame, the matrix ${}^d\mathbf{C}$ for an ideal spherical CM, expected to provide a purely spherical motion, should present finite (usually, as large as possible) lower-right diagonal terms (namely, $C_{\theta_x m_x}$, $C_{\theta_y m_y}$, $C_{\theta_z m_z}$), all the other terms being null. In case of practical (non-ideal) spherical CMs, a measure of the magnitude of all the other non-zero matrix entries can be used to assess the spherical CM behavior for what concerns undesired parasitic effects.

Compliance Matrix of a Single CFB

The CFB compliance matrix, previously obtained in [38] and recalled hereafter for the sake of clarity, when evaluated with respect to a reference frame S_0 centered at O_0 and with axes x_0, y_0, z_0 (i.e., parallel to those of primary compliance of each flexure, See Figure 3) takes the following form:

$${}^k\mathbf{C} = \begin{bmatrix} C_{xfx} & 0 & 0 & 0 & 0 & C_{xmz} \\ 0 & C_{yfy} & 0 & 0 & 0 & 0 \\ 0 & 0 & C_{z fz} & C_{zm_x} & 0 & 0 \\ 0 & 0 & C_{\theta_x fz} & C_{\theta_x m_x} & 0 & 0 \\ 0 & 0 & 0 & 0 & C_{\theta_y m_y} & 0 \\ C_{\theta_z fx} & 0 & 0 & 0 & 0 & C_{\theta_z m_z} \end{bmatrix}, \tag{3}$$

where:

$$\begin{aligned} C_{xfx} &= \frac{R[(\theta+S_\theta)(AR^2+I_n)]}{2EAI_n} & C_{yfy} &= -\frac{R[(S_\theta-\theta)(AR^2+I_n)]}{2EAI_n} \\ C_{xmz} &= C_{\theta_z fx} = \frac{2R^2S_{\theta/2}}{EI_n} & C_{z fz} &= \frac{R^3\theta}{GJ} \\ C_{zm_x} &= C_{\theta_x fz} = \frac{-2R^2S_{\theta/2}}{GJ} & C_{\theta_x m_x} &= \frac{R[GJ(\theta-S_\theta)+EI_m(\theta+S_\theta)]}{2EGJI_m} \\ C_{\theta_y m_y} &= -\frac{R[ES_\theta-\theta]I_m-GJ(\theta+S_\theta)}{2EGJI_m} & C_{\theta_z m_z} &= \frac{R\theta}{EI_n} \end{aligned}$$

having defined $S_\chi = \sin(\chi)$, $C_\chi = \cos(\chi)$ for a generic variable χ , whereas $R, \theta, w, t, A = wt, I_m = 1/12wt^3, I_n = 1/12tw^3, J = wt^3[1/3 - 0.21tw^{-1}(1 - 1/12t^4w^{-4})], E, \nu$, and $G = 1/2E(1 + \nu)^{-1}$ are, respectively, the CFB radius and subtended angle, the beam width, thickness, cross section area, area moments of inertia and torsional constant of the cross section, Young’s modulus, Poisson’s ratio, and shear modulus of the employed material. The torsional constant, J , has been obtained using the membrane analogy proposed in [47].

3. Compliance Matrix of the Compliant Spherical Joint

The compliant SJ studied in this paper is obtained by the in-parallel connection of two spherical serial chains (each formed by three CFBs), and can provide three rotational DoF between an input shaft (fixed) and an output shaft, as depicted in Figure 4a. Let us denote as Chain#1 (Figure 4b) and Chain#2 (Figure 4c), the upper and lower chains, respectively. As previously recalled, the compliance matrix of each serial chain can be simply obtained by summing up the compliance matrices of each beam, once all beam matrices are related to the common reference frame S_0 . Therefore, following the procedure explained in Section 2 and resorting to the methodology reported in [38], the compliance matrix of Chain#1 (Figure 4b) and Chain#2 (Figure 4c), respectively, take the forms:

$${}^0\mathbf{C}_{\text{Chain\#1}} = \begin{bmatrix} a & 0 & 0 & 0 & b & c \\ 0 & a & 0 & c & 0 & b \\ 0 & 0 & a & b & c & 0 \\ 0 & c & b & d & 0 & 0 \\ b & 0 & c & 0 & d & 0 \\ c & b & 0 & 0 & 0 & d \end{bmatrix}, \tag{4}$$

$${}^0\mathbf{C}_{\text{Chain\#2}} = \begin{bmatrix} a & 0 & 0 & 0 & -b & -c \\ 0 & a & 0 & -c & 0 & -b \\ 0 & 0 & a & -b & -c & 0 \\ 0 & -c & -b & d & 0 & 0 \\ -b & 0 & -c & 0 & d & 0 \\ -c & -b & 0 & 0 & 0 & d \end{bmatrix}, \quad (5)$$

where:

$$a = \frac{R\theta (I_n GJ + GJR^2 A + R^2 EAI_n)}{EAI_n GJ} \quad b = \frac{-2R^2 S_{\theta/2}}{GJ} \quad c = \frac{2R^2 S_{\theta/2}}{EI_n} \quad d = \frac{R\theta (I_n EI_m + I_n GJ + GJ I_m)}{GJ EI_m I_n}. \quad (6)$$

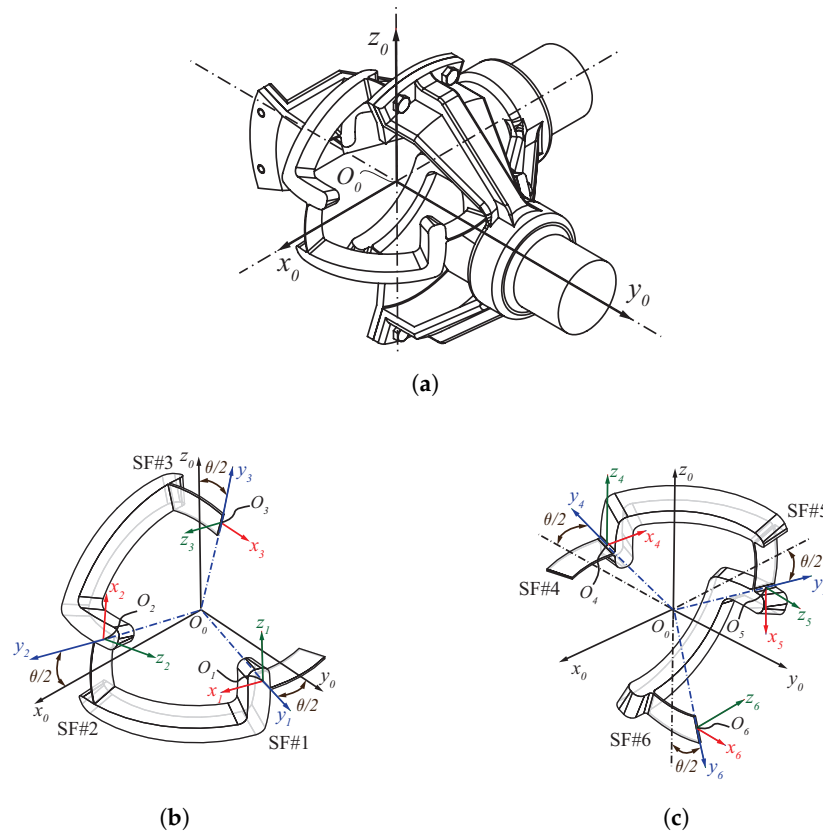


Figure 4. Compliant spherical joint (a) composed of two compliant serial chains, namely Chain#1 (b) and Chain#2 (c).

As one can notice, the compliance matrices of the chains are only a function of four independent factors, denoted as a , b , c and d .

A similar procedure can be adopted to obtain the overall SJ compliance matrix, considering the fact that, for parallel combinations, stiffness matrices of the chains should be summed up in the same reference frame. In this case, the following equation holds:

$${}^0\mathbf{K} = \sum_{i=1}^2 {}^0\mathbf{T}_i \cdot {}^i\mathbf{K} \cdot {}^0\mathbf{T}_i^T = {}^0\mathbf{C}_{\text{Chain\#1}}^{-1} + {}^0\mathbf{C}_{\text{Chain\#2}}^{-1}. \quad (7)$$

The SJ compliance matrix, ${}^0\mathbf{C}$, will then be obtained by inverting its stiffness matrix, ${}^0\mathbf{K}$, such that:

$${}^0\mathbf{C} = {}^0\mathbf{K}^{-1} = \begin{bmatrix} A & B & B & 0 & 0 & 0 \\ B & A & B & 0 & 0 & 0 \\ B & B & A & 0 & 0 & 0 \\ 0 & 0 & 0 & C & D & D \\ 0 & 0 & 0 & D & C & D \\ 0 & 0 & 0 & D & D & C \end{bmatrix}, \text{ where } \begin{matrix} A = \frac{1}{2} \frac{da-c^2-b^2}{d} & B = -\frac{1}{2} \frac{bc}{d} \\ C = \frac{1}{2} \frac{da-c^2-b^2}{a} & D = -\frac{1}{2} \frac{bc}{a} \end{matrix} \quad (8)$$

recalling a, b, c and d from Equation (6). Now, the matrix ${}^0\mathbf{C}$ may be diagonalized using a rigid body transformation. This procedure will simplify the optimization of the CFB geometric parameters, in order to maximize the SJ primary to secondary compliance factors. Let us denote with S_d a coordinate frame having an origin located on point O_0 , in which the SJ compliance matrix takes a diagonal form. The frame S_d is placed, with respect to frame S_0 , so that its orientation is represented by three Euler angles, α, β, γ , to be found, whereas its translation is trivially represented by three null parameters, namely $x_d = y_d = z_d = 0$. In this case, the diagonalized SJ compliance matrix, ${}^d\mathbf{C}$, can be retrieved resorting to the following equation:

$${}^d\mathbf{C} = {}^0\mathbf{T}_d^T \cdot {}^0\mathbf{C} \cdot {}^0\mathbf{T}_d, \text{ where } {}^0\mathbf{T}_d = \begin{bmatrix} {}^0\mathbf{R}_d & \mathbf{0} \\ \mathbf{0} & {}^0\mathbf{R}_d \end{bmatrix} \text{ and } {}^0\mathbf{R}_d = \begin{bmatrix} C_\alpha C_\beta & -S_\alpha C_\gamma + C_\alpha S_\beta S_\gamma & S_\alpha S_\gamma + C_\alpha S_\beta C_\gamma \\ S_\alpha C_\beta & C_\alpha C_\gamma + S_\alpha S_\beta S_\gamma & -C_\alpha S_\gamma + S_\alpha S_\beta C_\gamma \\ -S_\beta & C_\beta S_\gamma & C_\beta C_\gamma \end{bmatrix}. \quad (9)$$

By imposing null non-diagonal terms of ${}^d\mathbf{C}$ in Equation (9) and solving the three rotation angles, α, β, γ , the values $\alpha = \pi/4, \beta = \arctan(\sqrt{2})$ and $\gamma = 0$ are obtained, so that the matrix ${}^0\mathbf{R}_d$ is given by:

$${}^0\mathbf{R}_d = \begin{bmatrix} \nu\tau & -\nu & \tau \\ \nu\tau & \nu & \tau \\ -\frac{\nu\tau}{2} & 0 & \tau \end{bmatrix}, \text{ where } \begin{matrix} \nu = \frac{1}{2}\sqrt{2} \\ \tau = \frac{1}{3}\sqrt{3}. \end{matrix} \quad (10)$$

Resorting to Equations (9) and (10), the diagonalized SJ compliance matrix takes the following form:

$${}^d\mathbf{C} = \begin{bmatrix} -B + A & 0 & 0 & 0 & 0 & 0 \\ 0 & -B + A & 0 & 0 & 0 & 0 \\ 0 & 0 & 2B + A & 0 & 0 & 0 \\ 0 & 0 & 0 & -D + C & 0 & 0 \\ 0 & 0 & 0 & 0 & -D + C & 0 \\ 0 & 0 & 0 & 0 & 0 & 2D + C \end{bmatrix}. \quad (11)$$

Recalling Equations (6) and (8), it can be noticed that the parameters B and D are both positive in value, thus, $2B + A > -B + A$ and $2D + C > -D + C$, which implies that the terms ${}^dC_{33} = {}^dC_{z_fz}$ and ${}^dC_{66} = {}^dC_{\theta_z m_z}$ are, respectively, the largest secondary and primary compliance factors. In other words, to maximize the joint primary to secondary compliance factors and increase the joint spherical motion generation capabilities, the following ratio should be minimized:

$$r = \frac{{}^dC_{33}}{{}^dC_{44}} = \frac{2B + A}{-D + C} = \frac{(-2bc + da - c^2 - b^2) a}{d(bc + da - c^2 - b^2)}. \quad (12)$$

In order to perform a scale-independent parametric study, the curvature radius R of the CFBs is used as the characteristic size to obtain the dimensionless ratio $r^* = r/R^2$ that only depends on the flexure shape factors $w/t, w/R$ and θ . After performing parametric evaluations, within the limits of the slender beam approximation, the results show that r^* is almost independent of the relative width, w/R , so that its variation can be represented as a function of beam relative length (namely, θ) and

the cross-section aspect ratio (w/t) only. Exemplary numerical results are respectively depicted in Figure 5a,b. In these pictures, the black inclined straight lines (for given R/t ratios) are included in order to indicate the space of the geometric parameters that satisfy the slender beam approximation, the admissible geometries being those lying on the bottom-right side of the line. In particular, Figure 5a underlines the negligible influence of w/R on the parameter r^* for the case $w/t = 10$ (similar results also hold for different values of the cross-section aspect ratio w/t). In parallel, Figure 5b reports about the influence of w/t and θ on the same parameter. Overall, the results indicate that r^* can be minimized by selecting the largest feasible values for w/t and θ for which the flexible members can be considered as a slender beam.

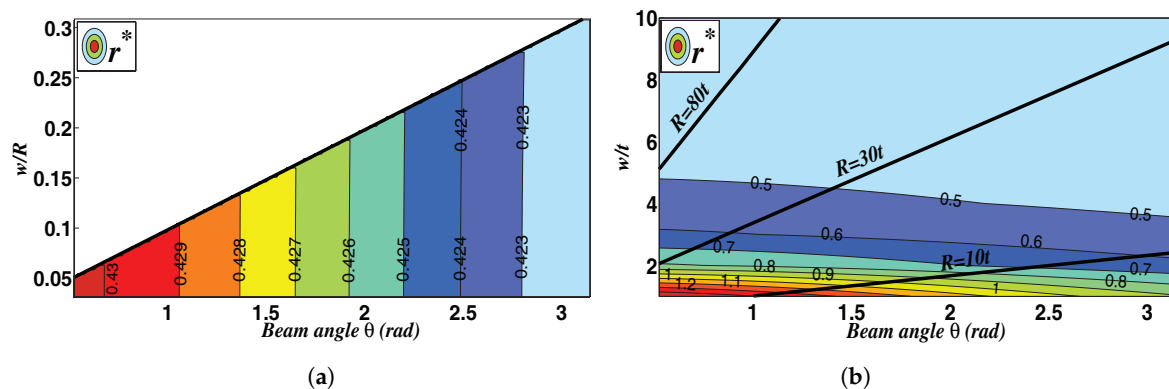


Figure 5. The influence of geometric parameters on the dimensionless ratio r^* : (a) influence of varying w/R and θ for $w/t = 10$, (b) influence of varying of w/t and θ . The inclined straight lines represent the limit space of admissible geometries employing the slender beam approximation.

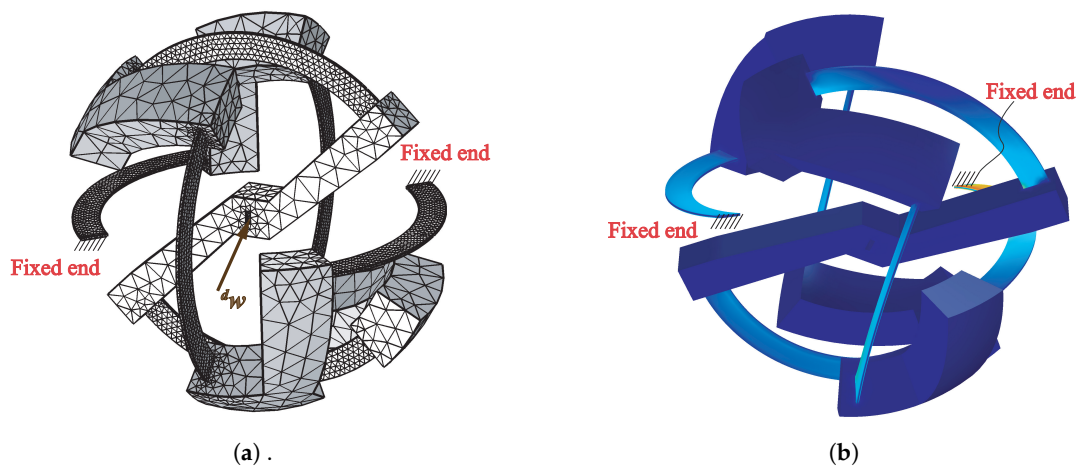
4. Numerical Example and Model Validation

4.1. Finite Element Analysis with a Small Deflection Hypothesis

The SJ compliance matrix computed via the analytical approach described in the previous section has been validated through three dimensional (3D) Finite Element Analysis (FEA) performed with the commercial software COMSOL 5.3. The considered flexure geometries are: $w = 10$ mm, $t = 1$ mm, $R = 65$ mm and $\theta = \pi/2$. The flexures are made from a metal material characterized by a Young's modulus $E = 200$ GPa and a Poisson's ratio $\nu = 0.33$. The Solid Stress-Strain application mode of the COMSOL Structural Mechanics Module has been used for the simulations. The global displacements in the x_d , y_d and z_d directions are the dependent variables in this application mode. The 3D solid model of the hinge is discretized using the automatic meshing routine available in the software. After a mesh convergence analysis, the final employed mesh is depicted in Figure 6a and consists of 15,572 tetrahedral elements and 30,310 nodes. Linear Elastic Material Model accounting for small deformations is chosen to ensure a linear relationship between stresses and deformations. FEA simulations are executed by individually loading the joint center in frame S_d along the x_d , y_d and z_d axes and by solving for the corresponding free-end deflections. The compliance factors are then computed as the ratios between each applied force or moment and the corresponding free-end displacements and rotations. Table 1 compares the results obtained via the analytical model described in the previous section and FEA. The comparison shows a close agreement between the two methods, thus validating the equations previously provided.

Table 1. Compliance factors for the spherical joint and comparison between analytical and FEA results

Compliance factors	${}^d C_{x_f x} = {}^d C_{y_f y} [\text{mN}^{-1}]$	${}^d C_{z_f z} [\text{mN}^{-1}]$	${}^d C_{\theta_x m_x} = {}^d C_{\theta_y m_y} [\text{m}^{-1} \text{N}^{-1}]$	${}^d C_{\theta_z m_z} [\text{m}^{-1} \text{N}^{-1}]$
Analytic	6.1980×10^{-4}	6.3279×10^{-4}	0.3505	0.3579
FEA	5.7876×10^{-4}	5.8937×10^{-6}	0.3428	0.3504
Percentage error (%)	6.6	6.8	2.2	2.1

**Figure 6.** Finite Element Analysis of the spherical joint: (a) model mesh and boundary conditions, (b) deformed shape under the application of large loads (i.e., $M_{y_d} = 2 \text{ Nm}$, $F_{x_d} = 20 \text{ N}$).

4.2. Finite Element Analysis with Large Deformation Hypothesis

A nonlinear FEA is further performed on the same SJ model to evaluate the joint behavior considering the large deflection hypothesis. This study is developed to assess the SJ properties when it is intended to undergo large motions and, in particular, rotations up to 45 degrees. Hence, the joint is loaded by large forces and moments, and the relationship between the loads and the deformations is not linear any longer. The nonlinear solver interface of COMSOL accounting for large deformations and geometric nonlinearities has been employed for the simulations. Mesh convergence analysis has been performed to guarantee minimum errors in iterative convergence computations of the software. The simulations have been executed by loading the joint center in frame S_d , along the x_d , y_d and z_d axes, and by solving for the corresponding free-end deflections. In order to obtain rotations up to 45 degrees, the joint has been loaded by moments with magnitude in the range of 0 to 2 Nm, with an incremental step size of “0.1 Nm”, and forces with magnitude in the range of 0 to 20 N, with an incremental step size of “1 N”. In particular, a single force/moment combination along either the x_d , y_d or z_d axes, is considered for each simulation to simply assess the joint motion along each individual axis. The total displacement of the joint center, δ (representing a parasitic motion or, in other words, a measure of the precision of rotation) has then been calculated to compare the results for different loading scenarios. In order to perform a scale-independent study, the curvature radius R of the CFBs is used as the characteristic size to obtain the dimensionless total displacement $\delta^* = \delta/R$, which turns useful for comparison purposes. Ideally, resorting to Equation (11), when the SJ is loaded by a pure moment along an individual axis of frame S_d , the joint should only provide a rotational motion along the same axis with no deformations along the other axes. However, in the large deflections regime, the SJ also exhibits undesired motions along the other axes. The angle-axis representation of three-dimensional rotations [48] is here used to quantify these parasitic rotations. For any spatial rotation, there exists a unique axis, Γ , about which the overall motion of the end link with respect to

its original frame can be defined by a single angle, ϕ . The following expressions hold for these axis and angle:

$$\phi = \cos^{-1}\left(\frac{r_{11} + r_{22} + r_{33} - 1}{2}\right), \quad (13)$$

$$\Gamma = \frac{1}{2 \sin \phi} \begin{bmatrix} r_{32} - r_{23} \\ r_{13} - r_{31} \\ r_{21} - r_{12} \end{bmatrix}, \quad (14)$$

where r_{ij} are the components of the rotation matrix, ${}^d\mathbf{R}_s$, between the joint deformed frame (hereafter referred to as frame S_s) and its original frame (frame S_d):

$${}^d\mathbf{R}_s = \begin{bmatrix} r_{11} & r_{12} & r_{13} \\ r_{21} & r_{22} & r_{23} \\ r_{31} & r_{32} & r_{33} \end{bmatrix}. \quad (15)$$

Resorting to Equations (13) and (15), the angle ϕ and the axis Γ are computed for each simulation step in order to evaluate the orientation of the SJ center when it is loaded by different force/moment combinations. Let us underline that ϕ represents the desired SJ rotation. In parallel, it is also desirable to assess parasitic rotations, defined by a second angle ψ , which represents the angle between the axis Γ and the axis on which the external moment is applied. The ratio ψ/ϕ is then used as a reference metric to compare parasitic rotations for each loading case.

Starting from the relation between parasitic displacements and desired rotations, simulations indicate that the total displacement of the joint center is mostly dependent on applied forces, whereas its rotation mainly depends on applied moments. In particular, Figure 7 demonstrates the variation of δ^* and ϕ for different loading cases in frame S_d . For instance, Figure 7a reports the variation of parameter δ^* when a constant external moment, $M_{y_d} = 2$ Nm, is applied along the y_d axis, whereas either forces F_{x_d} , F_{y_d} , F_{z_d} (in the range from 0 to 20 N) are applied on the respective axes. The same curves are also reported in Figure 7b, which however depicts all the possible loading-case combinations, namely, $M_{x_d}, M_{y_d}, M_{z_d} \in [0, 2]$ Nm and $F_{x_d}, F_{y_d}, F_{z_d}$ varying from 0 to 20 N. Since, for each moment load, 21 simulations have been performed (i.e., moments increasing from 0 to 2 Nm with increments of 0.1 Nm, as previously said), Figure 7b depicts the overlay of 63 curves in total. As one can notice, the dimensionless total displacement of the joint center increases almost linearly with increasing forces. A minimum δ^* measure is achieved for $M_{y_d} = 0$ Nm and a varying force, F_{z_d} , applied along the z_d axis. A maximum δ^* measure is achieved for $M_{y_d} = 2$ Nm and a varying force, F_{x_d} , applied along the x_d axis. In parallel, Figure 7c represents the quasi-linear dependency of the joint desired rotation ϕ as function of applied moments, namely $M_{x_d}, M_{y_d}, M_{z_d}$ varying from 0 to 2 Nm and parametric forces $F_{x_d}, F_{y_d}, F_{z_d} \in [0, 20]$ N, increasing with increments of 1 N (i.e., 63 curves in total). The minimum ϕ measure is obtained for $F_{z_d} = 0$ Nm and a varying moment, M_{y_d} , applied along the y_d axis, whereas the maximum ϕ measure is obtained for $F_{x_d} = 20$ N and a varying moment, M_{x_d} applied along the x_d axis. According to Figure 7b,c, there exists three *extreme* load cases scenarios for what concerns the measures δ^* and ϕ : (a) a combination of M_{y_d} and F_{x_d} (case of maximum parasitic displacement); (b) a combination of M_{x_d} and F_{x_d} (case of maximum desired rotation); (c) a combination of M_{y_d} and F_{z_d} (case of minimum desired rotation and minimum parasitic displacement). For the sake of clarity, it is recalled that all loads are applied to point O_o that is envisaged as the SJ center of spherical motion.

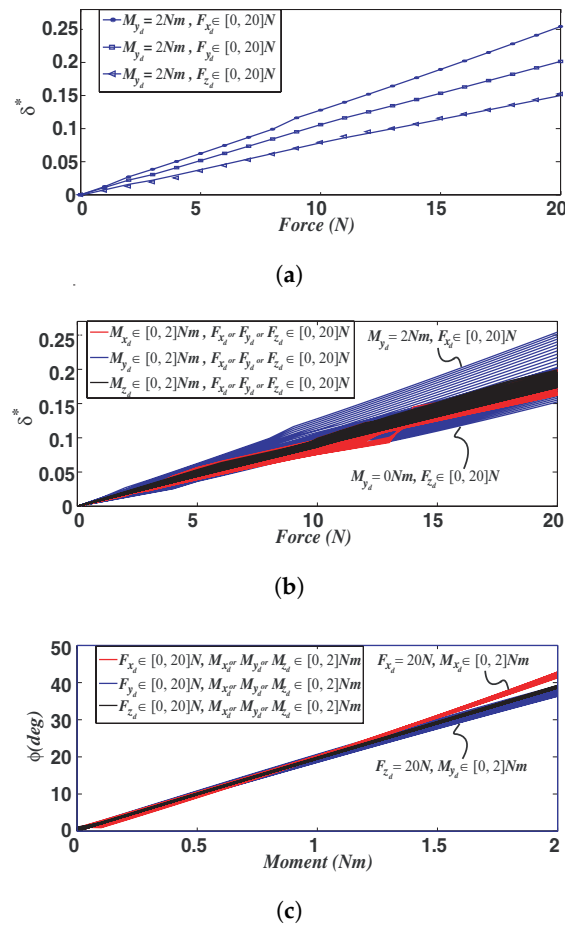


Figure 7. The variation of total parasitic displacement and desired rotation for different loading cases: (a) dimensionless total displacement variation for $M_{y_d} = 2Nm$ and applied force (either F_{x_d} , F_{y_d} , or F_{z_d}); (b) dimensionless total displacement variation for different loading cases in terms of applied force; (c) rotation variation for different loading cases in terms of applied moment.

For these three extreme loading cases, more detailed contour plots are represented in Figures 8–10. In particular, the contour plots of the dimensionless parasitic displacement δ^* in terms of moment and force are shown in Figure 8 for the three mentioned loading cases. As stated before, δ^* is mostly dependent on force variations (in fact, the curves are nearly horizontal), although a minor dependency on the applied moments can also be noticed. The relationship between δ^* and the applied moments is mostly dependent on the direction of the applied loads in frame S_d and how the SJ is deformed. For instance, for application of moment M_{y_d} and force F_{x_d} , as reported in Figure 8a, δ^* increases by increasing M_{y_d} . On the other hand, this relationship is inverse for the application of the same moment M_{y_d} , when the joint is contemporarily loaded by a force F_{z_d} , as shown in Figure 8b. A similar interpretation can be underlined for the SJ desired rotation with respect to the applied forces by comparing the rotation contour plots (namely parameter ϕ) depicted in Figure 9. In fact, in this case, the isolines are almost vertical. At last, the contour plots of the ratio ψ/ϕ , representing a measure of parasitic rotations, are illustrated in Figure 10. This picture clearly highlights that, for relatively high moment loads in any direction, a value of ψ/ϕ less than 0.25 can be achieved. This latter value increases whenever the moment loads decrease and the force loads increase (upper left corner of the plots). Finally, contour plots for all the other loading cases are reported in Appendix A, for the sake of completeness.

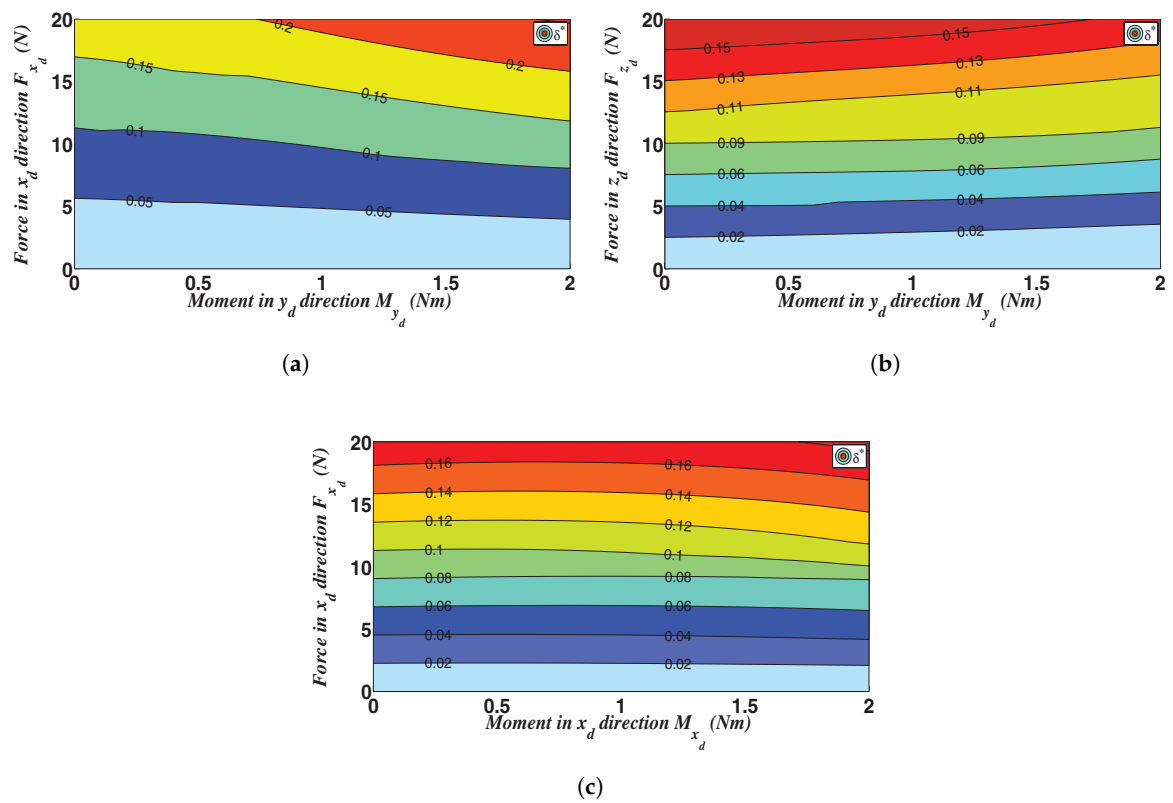


Figure 8. Contour plots of δ^* for three extreme loading cases: (a) moment M_{y_d} and force F_{x_d} ; (b) moment M_{y_d} and force F_{z_d} ; (c) moment M_{x_d} and force F_{x_d} .

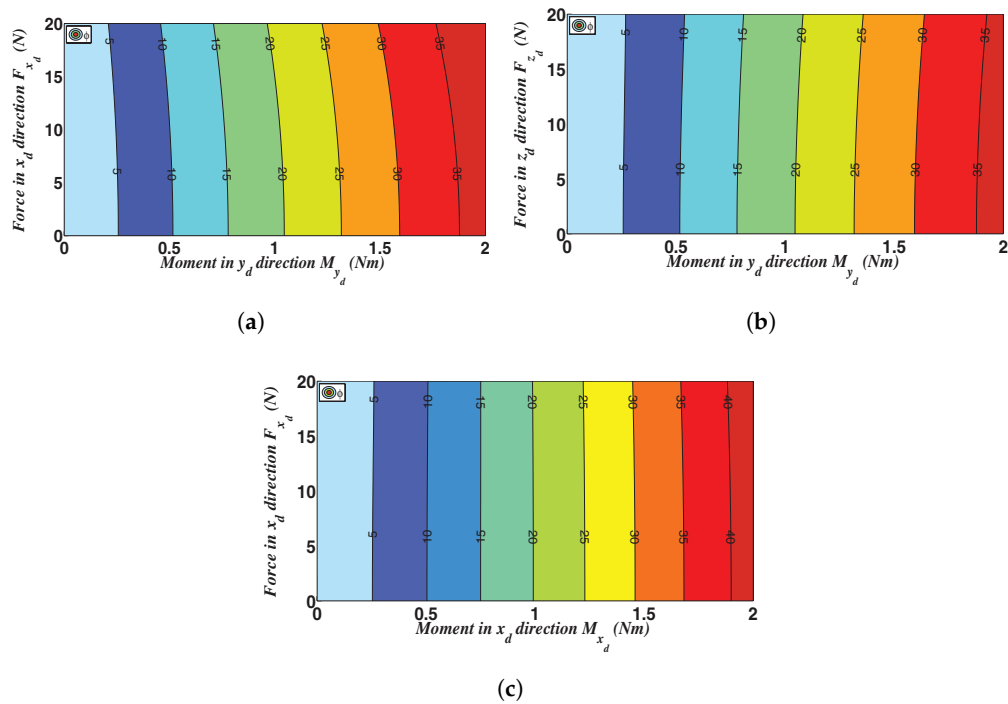


Figure 9. Contour plots of ϕ for three extreme loading cases: (a) moment M_{y_d} and force F_{x_d} ; (b) moment M_{y_d} and force for F_{z_d} ; (c) moment M_{x_d} and force F_{x_d} .

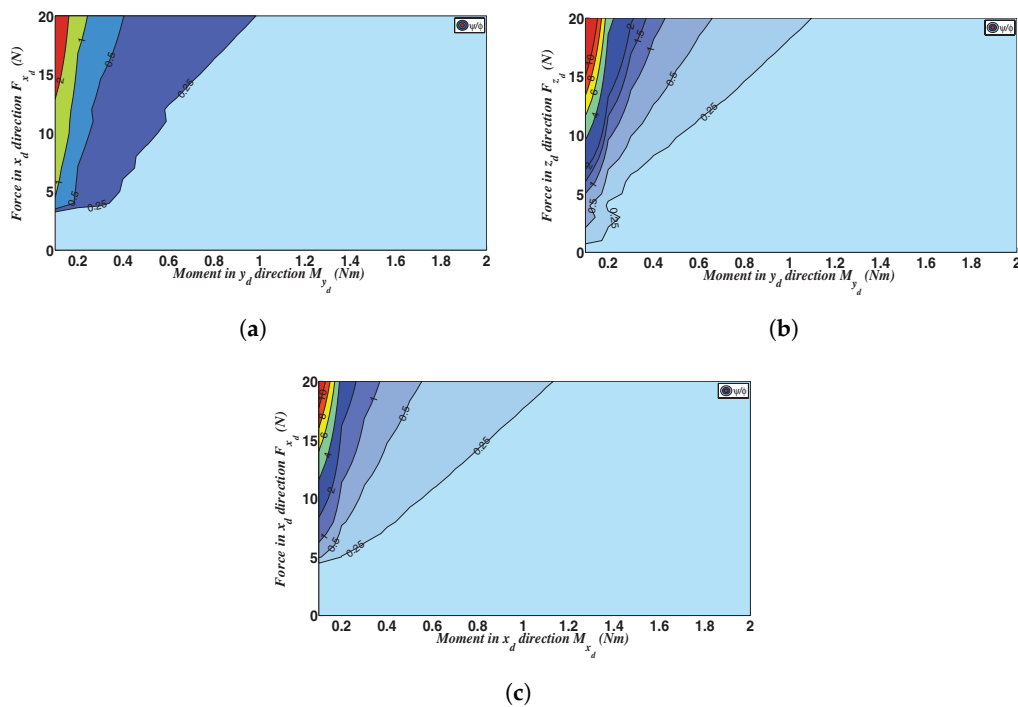


Figure 10. Contour plots of ψ/ϕ for three extreme loading cases: (a) moment M_{y_d} and force F_{x_d} ; (b) moment M_{y_d} and force F_{z_d} ; (c) moment M_{x_d} and force F_{x_d} .

5. Conclusions

The design of a compliant joint, suitable for realizing approximately spherical motions and featuring two open chains connected in parallel, has been introduced and analyzed. Each chain is composed by the in-series connection of three identical circular flexible beams with coincident centers of curvature and mutually orthogonal axes of maximum rotational compliance. First, the closed form compliance equations of the proposed spherical joint have been presented as a function of the beam dimensions and employed material. It has been shown that, within the small deformation range, the joint can provide an isotropic behavior, its compliance matrix being diagonal. Then, a parametric study has been conducted based on the equations obtained from the theoretical approach, in order to optimize the beam geometric parameters allowing to maximize the primary to secondary compliance factors. Finite element analysis has been subsequently performed, both within the small deflection hypothesis (in order to validate the results obtained from the theoretical approach), and for large deflection hypothesis (in order to evaluate the joint behavior when it is intended to undergo large rotations subjected to large loads). Thanks to its isotropism (in absence of external loads other than the primary moments), this joint design seems interesting for implementing high-precision spherical mechanisms and robotic actuated devices formed therewith. Naturally, due to the chosen topology, the joint center may be affected by undesired translations. Nonetheless, this latter issue may be mitigated by implementing the concept of contact-aided compliant mechanism (i.e., by introducing contact surfaces that mitigate the presence of parasitic motions). Future developments include manufacturing and testing of a physical joint prototype in either plastic or metal materials.

Author Contributions: Farid Parvari Rad performed FEA simulations and contributed to analytical model development. Giovanni Berselli, Rocco Vertechy and Vincenzo Parenti Castelli propped the joint design, contributed to the analytical model and supervised the project. All authors wrote the paper.

Funding: This research was funded by the Italian Minister of Education and Research via Ph.D. grants

Acknowledgments: No acknowledgments to declare.

Conflicts of Interest: The authors declare no conflict of interest.

Appendix A. Supplementary Plots

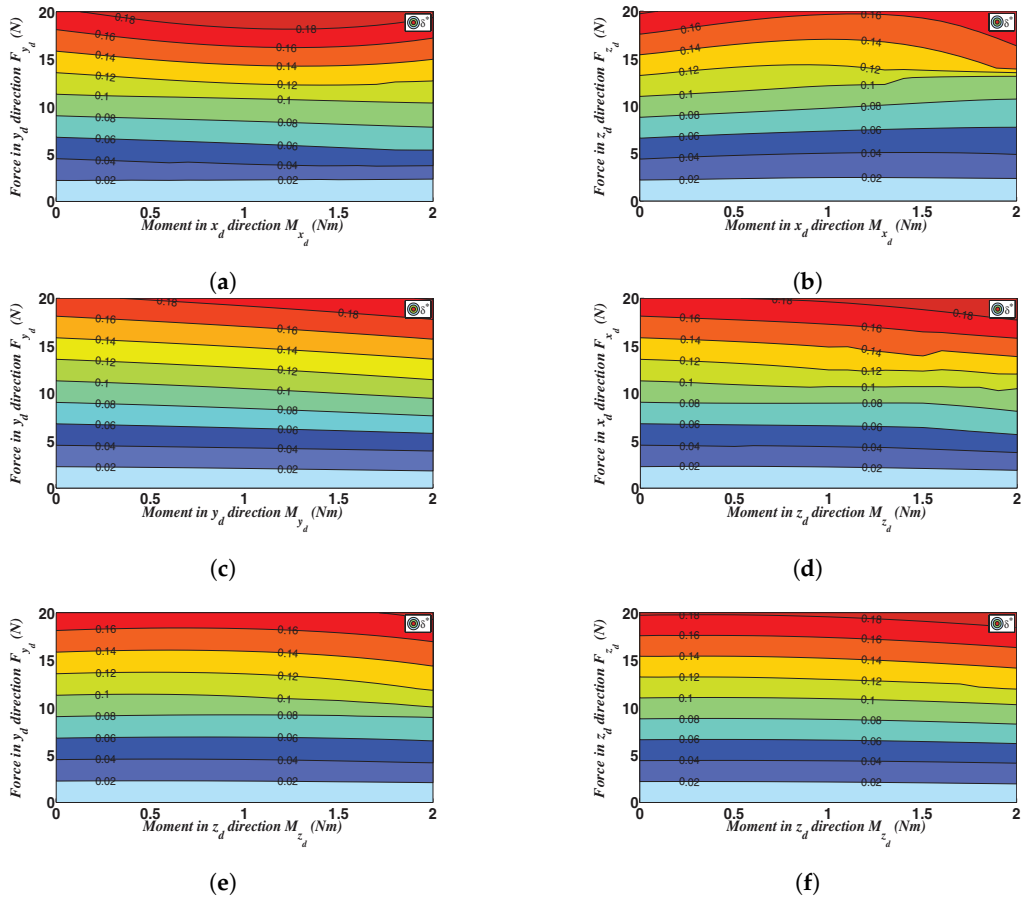


Figure A1. Contour plots of δ^* for all the loading cases: (a) moment, M_{x_d} , and force, F_{y_d} ; (b) moment, M_{x_d} , and force, F_{z_d} ; (c) moment, M_{y_d} , and force, F_{y_d} ; (d) moment, M_{z_d} , and force, F_{x_d} ; (e) moment, M_{z_d} , and force, F_{y_d} ; (f) moment, M_{z_d} , and force, F_{z_d} .

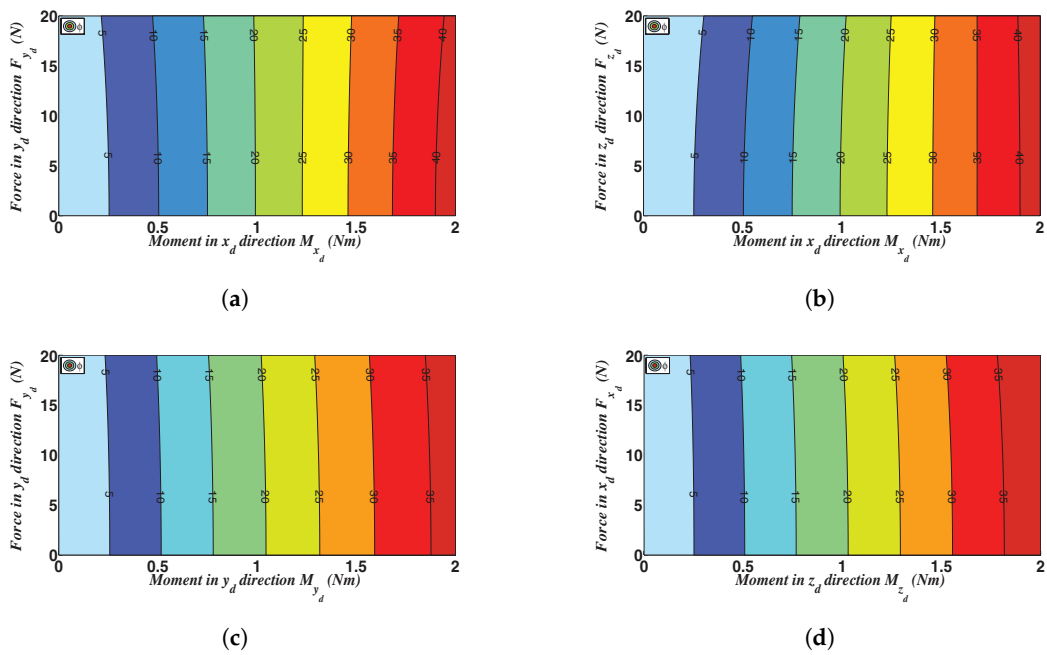
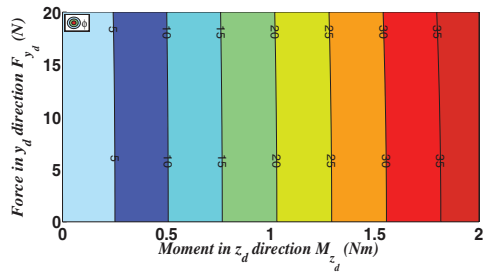
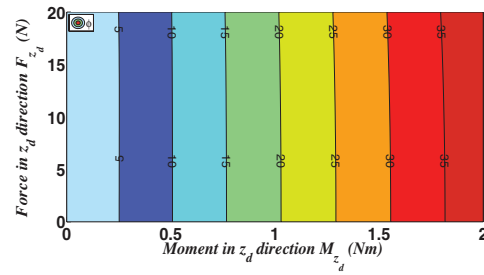


Figure A2. Cont.

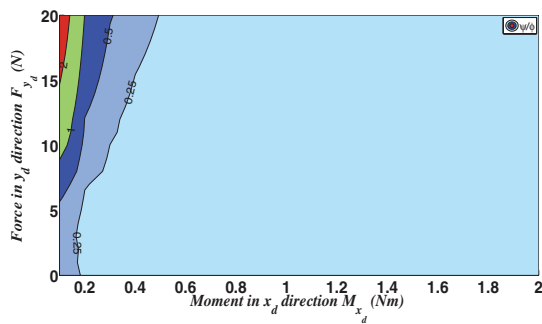


(e)

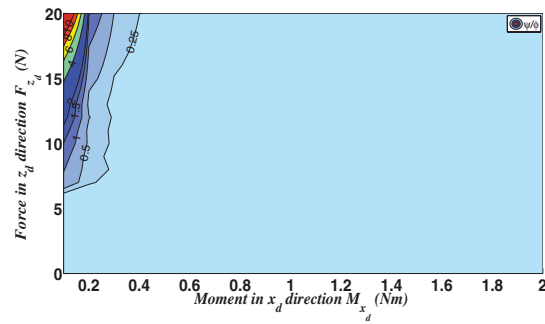


(f)

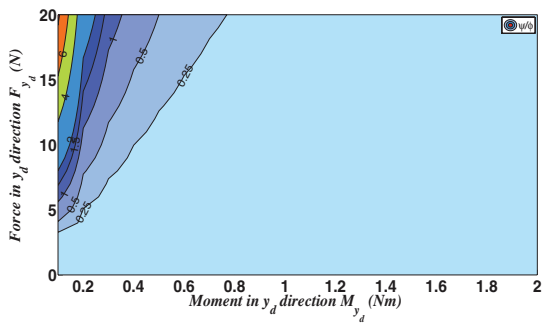
Figure A2. Contour plots of ϕ for all the loading cases: (a) moment, M_{x_d} , and force, F_{y_d} ; (b) moment, M_{x_d} , and force, F_{z_d} ; (c) moment, M_{y_d} , and force, F_{y_d} ; (d) moment, M_{z_d} , and force, F_{x_d} ; (e) moment, M_{z_d} , and force, F_{y_d} ; (f) moment, M_{z_d} , and force, F_{z_d} .



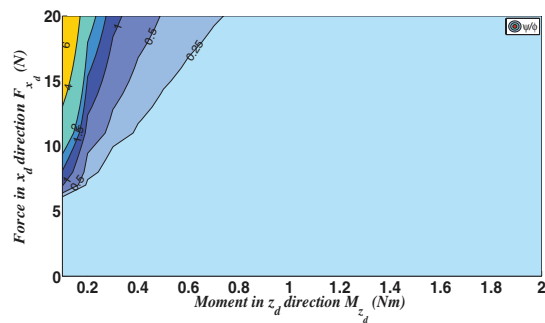
(a)



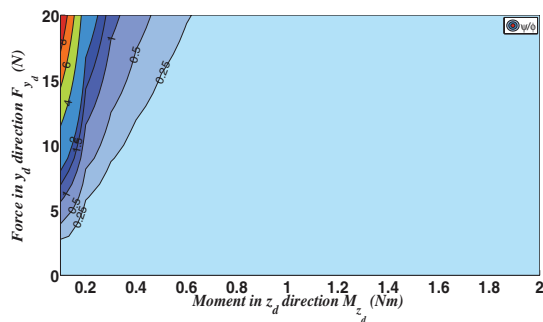
(b)



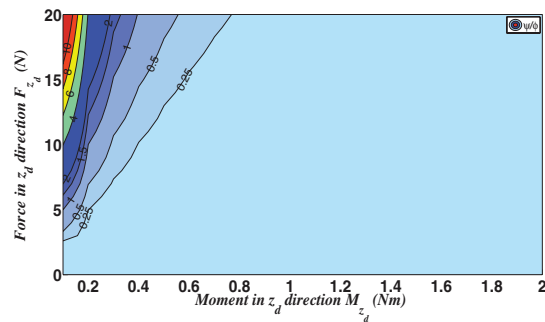
(c)



(d)



(e)



(f)

Figure A3. Contour plots of ψ/ϕ for all the loading cases: (a) moment, M_{x_d} , and force, F_{y_d} ; (b) moment, M_{x_d} , and force, F_{z_d} ; (c) moment, M_{y_d} , and force, F_{y_d} ; (d) moment, M_{z_d} , and force, F_{x_d} ; (e) moment, M_{z_d} , and force, F_{y_d} ; (f) moment, M_{z_d} , and force, F_{z_d} .

References

1. Howell, L.L. *Compliant Mechanisms*; Wiley: New York, NY, USA, 2001.
2. Lu, K.-J. Synthesis of Shape Morphing Compliant Mechanisms. Ph.D. Thesis, University of Michigan, Ann Arbor, MI, USA, 2004.
3. Hesselbach, J.; Wrege, J.; Raatz, A.; Becker, O. Aspects on design of high precision parallel robots. *Assem. Autom.* **2004**, *24*, 49–57.
4. Erkaya, S.; Doğan, S.; Ulus, S. Effects of joint clearance on the dynamics of a partly compliant mechanism: Numerical and experimental studies. *Mech. Mach. Theory* **2015**, *88*, 125–140.
5. Ouyang, P.R.; Tjiptoprodjo, R.C.; Zhang, W.J.; Yang, G.S. Micro-motion devices technology: The state of arts review. *Int. J. Adv. Manuf. Technol.* **2008**, *38*, 463–478.
6. Soemers, H. *Design Principles for Precision Mechanisms*; T-Pointprint: Enschede, The Netherlands, 2010.
7. Palli, G.; Melchiorri, C.; Berselli, G.; Vassura, G. Design and modeling of variable stiffness joints based on compliant flexures. In Proceedings of the 34th Annual Mechanisms and Robotics Conference, Montreal, QC, Canada, 15–18 August 2010; Volume 2, pp. 1069–1078.
8. Borboni, A.; Faglia, R.; Mor, M. Compliant device for hand rehabilitation of stroke patient. In Proceedings of the ASME 12th Biennial Conference on Engineering Systems Design and Analysis, Copenhagen, Denmark, 25–27 July 2014; Volume 1, p. V001T03A001.
9. Borboni, A.; Faglia, R. Robust design of a shape memory actuator with slider and slot layout and passive cooling control. *Microsyst. Technol.* **2018**, *24*, 1379–1389.
10. Scarfogliero, U.; Stefanini, C.; Dario, P. The use of compliant joints and elastic energy storage in bio-inspired legged robots. *Mech. Mach. Theory* **2009**, *44*, 580–590.
11. Ham, R.V.; Sugar, T.G.; Vanderborght, B.; Hollander, K.W.; Lefeber, D. Compliant actuator designs. *IEEE Robot. Autom. Mag.* **2009**, *16*, 81–94.
12. Wang, D.H.; Yang, Q.; Dong, H.M. A monolithic compliant piezoelectric-driven microgripper: Design, modeling, and testing. *IEEE/ASME Trans. Mechatron.* **2013**, *18*, 138–147.
13. Reddy, B.N.; Naik, S.; Saxena, A. Systematic synthesis of large displacement contact-aided monolithic compliant mechanisms. *ASME J. Mech. Des.* **2012**, *134*, 011007.
14. Teo, T.J.; Yang, G.; Chen, I. Compliant manipulators. In *Handbook of Manufacturing Engineering and Technology*; Springer: London, UK, 2014; pp. 1–63.
15. Gao, Z.; Zhang, D. Workspace representation and optimization of a novel parallel mechanism with three-degrees-of-freedom. *Sustainability* **2011**, *3*, 2217–2228.
16. Guo, K.; Ni, M.; Chen, H.; Sui, Y. A monolithic adjusting mechanism for optical element based on modified 6-pss parallel mechanism. *Sens. Actuators A Phys.* **2016**, *251*, 1–9.
17. Palmieri, G.; Palpacelli, M.C.; Callegari, M.M. Study of a fully compliant u-joint designed for minirobotics applications. *ASME J. Mech. Des.* **2012**, *134*, 111003.
18. Berselli, G.; Guerra, A.; Vassura, G.; Andrisano, A. An engineering method for comparing selectively compliant joints in robotic structures. *IEEE/ASME Trans. Mechatron.* **2014**, *19*, 1882–1895.
19. Lobontiu, N.; Paine, J. Design of circular cross-section corner-filleted flexure hinges for three-dimensional compliant mechanisms. *J. Mech. Des. Trans. ASME* **2002**, *124*, 479–484.
20. Lobontiu, N. *Compliant Mechanisms: Design of Flexure Hinges*; CRC Press: Boca Raton, FL, USA, 2002.
21. Borboni, A.; Faglia, R. *Parasitic Phenomena in the Dynamics of Industrial Devices*; CRC Press: Boca Raton, FL, USA, 2017.
22. Coiffet, P. *Les Robots: Modelisation et Commande*; Hermes Publishing: Hunt Valley, MD, USA, 1981.
23. Berselli, G.; Parvari Rad, F.; Vertechy, R.; Parenti-Castelli, V. Comparative evaluation of straight and curved beam flexures for selectively compliant mechanisms. In Proceedings of the 2013 IEEE/ASME International Conference on Advanced Intelligent Mechatronics (AIM), Wollongong, NSW, Australia, 9–12 July 2013; pp. 1761–1766.
24. Hasse, A.; Campanile, L.F. Design of compliant mechanisms with selective Compliance. *Smart Mater. Struct.* **2009**, *18*, 115016.
25. Yin, L.; Ananthasuresh, G.K. Design of distributed compliant mechanisms. *Mech. Based Des. Struct. Mach.* **2003**, *31*, 151–179.

26. Meng, Q.; Li, Y.; Xu, J. New empirical stiffness equations for corner-filletted flexure hinges. *Mech. Sci.* **2013**, *4*, 345–356.
27. Lobontiu, N.; Paine, J.; Garcia, E.; Goldfarb, M. Design of symmetric conic-section flexure hinges based on closed-form compliance equations. *Mech. Mach. Theory* **2002**, *37*, 477–498.
28. Berselli, G.; Meng, Q.; Vertechy, R.; Parenti-Castelli, V. An improved design method for the dimensional synthesis of flexure-based compliant mechanisms: Optimization procedure and experimental validation. *Meccanica* **2016**, *51*, 1209–1225.
29. Chen, G.; Liu, X.; Du, Y. Elliptical-arc-fillet flexure hinges: Toward a generalized model for commonly used flexure hinges. *J. Mech. Des.* **2011**, *133*, 081002.
30. Liu, M.; Zhang, X.; Fatikow, S. Design and analysis of a high-accuracy flexure Hinge. *Rev. Sci. Instrum.* **2016**, *87*, 055106.
31. Zhu, B.; Zhang, X.; Fatikow, S. Design of single-axis flexure hinges using continuum topology optimization method. *Sci. China Technol. Sci.* **2014**, *57*, 560–567.
32. Meirovitch, L. *Elements of Vibration Analysis*; McGraw Hill: New York, NY, USA, 1986.
33. Parvari Rad, F.; Vertechy, R.; Berselli, G.; Parenti-Castelli, V. Compliant serial 3R chain with spherical flexures. *Adv. Robot Kinemat.* **2018**, *2016*, 11–21.
34. Smith, C.; Lusk, C. Modeling and parameter study of bistable spherical compliant Mechanisms. In Proceedings of the ASME Design Engineering Technical Conference, Washington, DC, USA, 28–31 August 2011; Volume 6, pp. 51–58.
35. Wilding, S.E.; Howell, L.L.; Magleby, S.P. Spherical lamina emergent mechanisms. *Mech. Mach. Theory* **2012**, *49*, 187–197.
36. Tanık, Ç.M.; Parlaktas, V.; Tanık, E.; Kadioğlu, S. Steel compliant cardan universal joint. *Mech. Mach. Theory* **2015**, *92*, 171–183.
37. Farhadi Machekposhti, D.; Tolou, N.; Herder, J.L. The scope for a compliant homokinetic coupling based on review of compliant joints and rigid-body constant velocity universal joints. In Proceedings of the ASME IDETC International Design Engineering Technical Conferences, Chicago, IL, USA, 12–15 August 2012; Volume 4, pp. 379–392.
38. Parvari Rad, F.; Vertechy, R.; Berselli, G.; Parenti-Castelli, V. Analytical compliance analysis and finite element verification of spherical flexure hinges for spatial compliant mechanisms. *Mech. Mach. Theory* **2016**, *101*, 168–180.
39. Parvari Rad, F.; Berselli, G.; Vertechy, R.; Parenti-Castelli, V. Design and stiffness analysis of a compliant spherical chain with three degrees of freedom. *Precis. Eng.* **2017**, *47*, 1–9.
40. Berselli, G.; Vassura, G.; Piccinini, M. Comparative evaluation of the selective compliance in elastic joints for robotic structures. In Proceedings of the IEEE ICRA International Conference on Robotics and Automation, Shanghai, China, 9–13 May 2011; pp. 759–764.
41. Mankame, N.D.; Ananthasuresh, G.K. Contact aided compliant mechanisms: Concept and preliminaries. In Proceedings of the ASME IDETC, International Design Engineering Technical Conferences, Montreal, QC, Canada, 29 September–2 October 2002; Volume 5, pp. 109–121.
42. Cannon, J.R.; Howell, L.L. A compliant contact-aided revolute joint. *Mech. Mach. Theory* **2005**, *40*, 1273–1293.
43. Carter Hale, L. Principles and Techniques for Designing Precision Machines. Ph.D. Thesis, Department of Mechanical Engineering, MIT, Cambridge, MA, USA, 1999.
44. Loncaric, J. Normal forms of stiffness and compliance matrices. *IEEE J. Robot. Autom.* **1987**, *3*, 567–572, doi:10.1109/JRA.1987.1087148.
45. Howard, S.; Zefran, M.; Kumar, V. On the 6x6 cartesian stiffness matrix for three-dimensional motions. *Mech. Mach. Theory* **1998**, *33*, 389–408.
46. Zhang, S.; Fasse, E.D. A finite-element-based method to determine the spatial stiffness properties of a notch hinge. *ASME J. Mech. Des.* **2001**, *123*, 141–147.
47. Timoshenko, S.; Goodier, J. *Theory of Elasticity, Vol. 412*; McGraw Hill: New York, NY, USA, 1951.
48. Siciliano, B.; Sciavicco, L.; Villani, L.; Oriolo, G. *Robotics: Modelling, Planning and Control*; Springer: New York, NY, USA, 2010.

